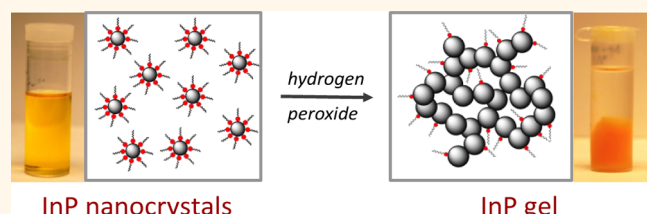


# Assembly of Phosphide Nanocrystals into Porous Networks: Formation of InP Gels and Aerogels

Asha Hitihami-Mudiyanselage, Keerthi Senevirathne, and Stephanie L. Brock\*

Department of Chemistry, Wayne State University, Detroit, Michigan 48202, United States

**ABSTRACT** The applicability of sol–gel nanoparticle assembly routes, previously employed for metal chalcogenides, to phosphides is reported for the case of InP. Two different sizes (3.5 and 6.0 nm) of InP nanoparticles were synthesized by solution-phase arrested precipitation, capped with thiolate ligands, and oxidized with H<sub>2</sub>O<sub>2</sub> or O<sub>2</sub>/light to induce gel formation. The gels were aged, solvent-exchanged, and then supercritically dried to obtain aerogels



with both meso- (2–50 nm) and macropores (>50 nm) and accessible surface areas of  $\sim 200 \text{ m}^2/\text{g}$ . Aerogels showed higher band gap values relative to precursor nanoparticles, suggesting that during the process of assembling nanoparticles into 3D architectures, particle size reduction may have taken place. In contrast to metal chalcogenide gelation, InP gels did not form using tetranitromethane, a non-oxygen-transferring oxidant. The requirement of an oxygen-transferring oxidant, combined with X-ray photoelectron spectroscopy data showing oxidized phosphorus, suggests gelation is occurring due to condensation of phosphorus oxoanionic moieties generated at the interfaces. The ability to link discrete InP nanoparticles into a 3D porous network while maintaining quantum confinement is expected to facilitate exploitation of nanostructured InP in solid-state devices.

**KEYWORDS:** InP · gels · aerogels · III–V semiconductors · quantum confinement

**A**erogels are an important class of nanostructured materials consisting of nanoscale building blocks that are interconnected, leading to a porous network structure. Because of the unique physical nature of aerogels, they have a wide range of applications as catalysts, adsorbents, and thermal insulators. Aerogel compositions were traditionally focused on oxides, especially SiO<sub>2</sub>, but expanded to embrace carbon in the 1990s.<sup>1–6</sup> In 2004, metal chalcogenide (MQ) aerogels were reported for the first time *via* supercritical drying of gels produced by a nanoparticle assembly route in which discrete nanoparticles were capped with a thiolate ligand, followed by controlled oxidative removal of the ligand to form a gel.<sup>7</sup> The interparticle linkages in the gel network were found to consist of catenated chalcogenides, a result of oxidation of surface Q<sup>2–</sup> to form bridging (Q<sub>n</sub>)<sup>2–</sup> ( $n \geq 2$ ) species between particles. This approach has been extended to a wide range of compositions, including CdS, PbS, ZnS, CdSe, and CdTe.<sup>8–10</sup> Since our original report, alternative approaches have also appeared, extending the compositions

and morphologies of chalcogenide aerogels that can be produced.<sup>11–19</sup>

An untapped element of the periodic table *vis à vis* sol–gel chemistry is phosphorus. Phosphorus has a great propensity to catenate into chains, rings, and clusters. There are numerous examples of binary (M<sub>4</sub>P<sub>6</sub> where M = K, Rb, Cs, Rb<sub>3</sub>P<sub>7</sub>, and Cu<sub>2</sub>P<sub>20</sub>) and ternary metal polyphosphides (Cu<sub>5</sub>InP<sub>16</sub>) featuring P–P bonds.<sup>20,21</sup> Therefore, it should be feasible to produce linkages *via* P–P bond formation at the nanoparticle interfaces by chemical oxidation, analogous to what is done with chalcogenides. This would open the door to a new class of materials unprecedented in the literature. Here we demonstrate the efficacy of oxidative gelation of nanoparticle networks of phosphides, specifically InP.

InP is a direct band gap semiconductor that has a bulk band gap value of 1.35 eV and Bohr excitonic diameter of 15 nm, which gives a large window for tuning particle size and, hence, the optical properties (CdSe has a 7.5 nm Bohr excitonic diameter).<sup>22</sup> Thus, InP-based nanowires have been evaluated as components in field effect transistors,

\* Address correspondence to sbrock@chem.wayne.edu.

Received for review September 16, 2012 and accepted January 24, 2013.

Published online January 24, 2013  
10.1021/nn305959q

© 2013 American Chemical Society

photodetectors, light-emitting diodes, and solar cell materials.<sup>23–25</sup> In contrast, no work has been reported on sol–gel assembly for generation of InP nanostructures. The ability to connect InP nanoparticles in 3D, while maintaining accessibility *via* the pore network, is expected to enhance the utility of InP nanostructures for applications benefiting from connectivity, openness, and interfacial interactions with complementary components (e.g., sensing, photocatalysis, hybrid photovoltaics).

## RESULTS AND DISCUSSION

The gel network formation mechanism for thiolate (11-mercaptoundecanoic acid)-capped CdSe nanoparticles has been reported by Brock and co-workers.<sup>26</sup> The assembly appears to be held together by interparticle Se–Se bonds that form due to oxidation of surface Se<sup>2+</sup> species. The process of gelation can accordingly be reversed by reduction of Se–Se bonds using agents such as thiols, leading to dispersion. This mechanism appears to extend to all metal chalcogenides (i.e., Q–Q bonds are responsible for gel networks). If we consider a similar mechanism for metal phosphide particles, as shown in Figure 1a, thiolates on the surface of the nanoparticles will be oxidized to form disulfides, which will leave the surface of the particles exposed to the oxidant. Subsequent solubilization of metal ions will result in a surface rich in P<sup>3–</sup> species. If oxidation of P<sup>3–</sup> species occurs analogously to S, Se, and Te, we expect to see formation of P–P bonds, *e.g.*, P<sub>2</sub><sup>4–</sup>. Such P<sub>2</sub><sup>4–</sup> species are well established in the solid-state chemistry of phosphides.<sup>27</sup> While there is no precedent for a binary indium polyphosphide phase, In can coexist with polyphosphides, as seen in the ternary phase Cu<sub>5</sub>Ind<sub>16</sub>, suggesting the proposed route should be feasible.<sup>20</sup>

To test this hypothesis, we prepared thiolate-capped InP nanoparticles and evaluated their propensity toward gelation in the presence of oxidants. Briefly, InP nanoparticles capped with trioctylphosphine oxide (TOPO) were prepared by solution-phase arrested precipitation following reported methods in the literature with slight modifications. The TOPO ligands on the InP nanoparticle surface were subsequently exchanged with 11-mercaptoundecanoic acid (MUA). Upon treatment with 3% H<sub>2</sub>O<sub>2</sub>, we observed the initiation of gel formation within approximately 30 min (Figure 2). Moreover, capped sols left under ambient fluorescent lighting in the lab also yielded gels, but this process is slow and takes approximately 3 weeks before gel formation becomes apparent. Presumably, in the latter case gelation is occurring by photooxidation with O<sub>2</sub> from air, consistent with our previous work on chalcogenide gels.<sup>8</sup> The gels were aged for 10–14 days to provide the gel network more mechanical integrity, and then the mother liquor was thoroughly exchanged with acetone, taking care not to disturb the gel network. Supercritical drying was employed to maintain

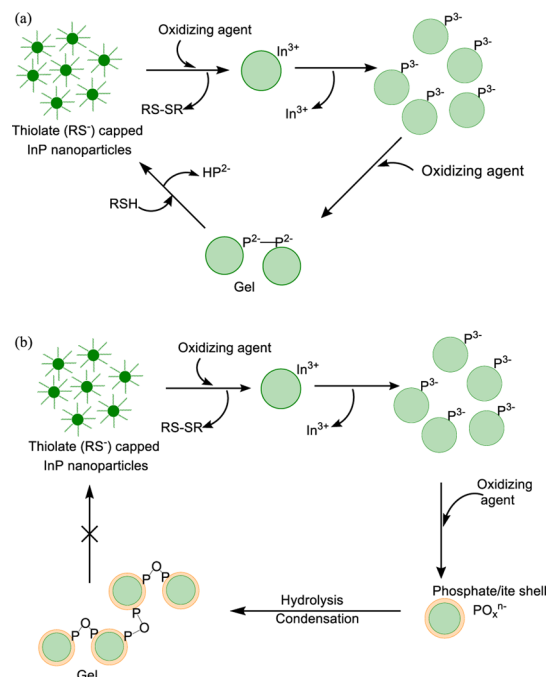


Figure 1. (a) Initial hypothesis for metal phosphide gel network formation and (b) modified hypothesis.

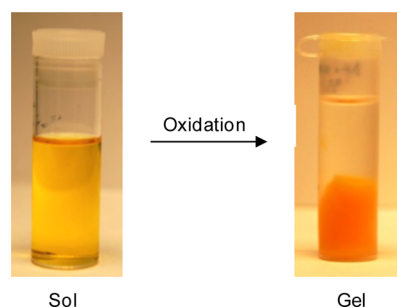


Figure 2. Gelation of a sol of InP nanoparticles upon introduction of the oxidant, 3% H<sub>2</sub>O<sub>2</sub>.

the pore structure in the solid state, generating an aerogel.

### Structure and Morphology of InP Nanoparticles and Aerogels.

InP aerogels (AG) are crystallographically identical to the nanoparticles from which they were assembled. Structural-phase identification was carried out using powder X-ray diffraction (PXRD). The PXRD patterns of InP nanoparticles (NP) of two different sizes are shown in Figure 3a and b. There are three distinct peaks that correlate to the expected pattern for cubic InP. The peaks are broad, consistent with formation of nanoparticles. Crystallite sizes were calculated by applying the Scherrer formula to the (220) peak. The calculated particle sizes were  $3.5 \pm 0.2$  nm for a single precursor injection synthesis and  $6.0 \pm 0.3$  nm for a synthesis employing multiple injections of precursor.

InP aerogels display the distinctive pearl necklace morphology of colloidal aggregates, similar to base-catalyzed silica gels. Transmission electron microscopy

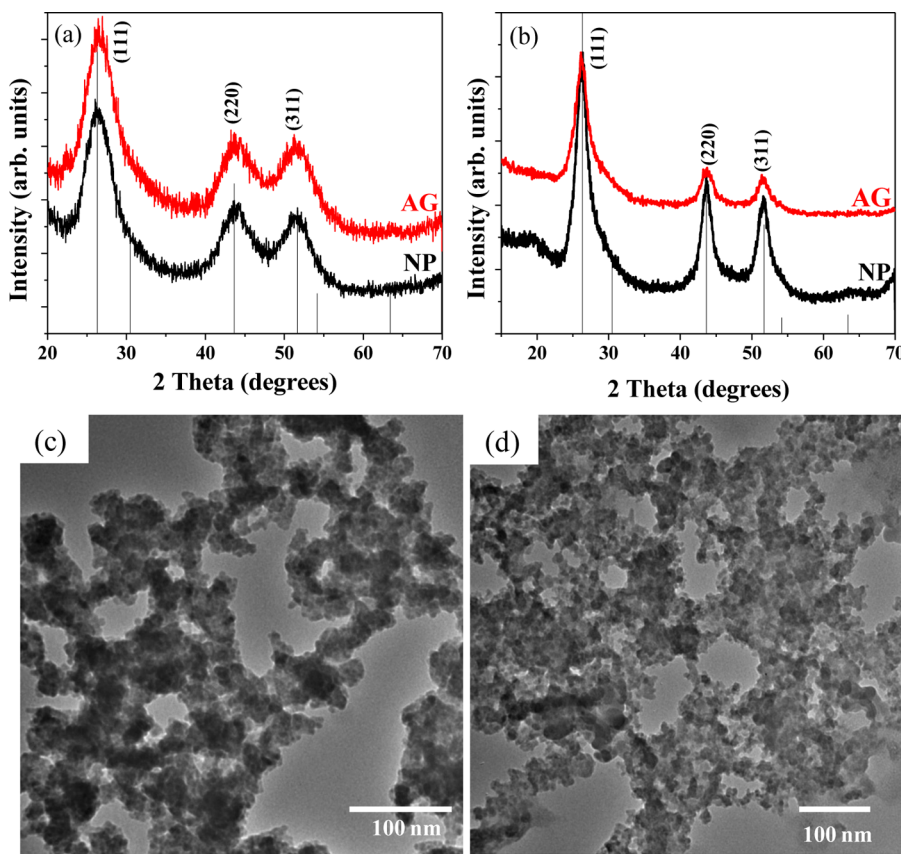


**Figure 3.** PXRD patterns of (a) 3.5 and (b) 6.0 nm InP nanoparticles (NP) and their aerogels (AG). The ICDD-PDF overlay of InP (PDF #32-0452) is shown as vertical lines in (a) and (b). TEM micrographs of AGs prepared from (c) 3.5 and (d) 6.0 nm InP NPs.

(TEM) was used to study the morphology of InP nanoparticles and aerogels. TEM micrographs of 3.5 and 6.0 nm InP nanoparticles are shown in Figure S1 in the Supporting Information. Both samples of nanoparticles are narrowly polydisperse and showed average sizes of  $4.0 \pm 0.9$  and  $8.0 \pm 0.9$  nm, slightly larger than values obtained by application of the Scherrer formula to the PXRD data (from this point forward when referring to the particle size, the sizes computed from the Scherrer formula will be used). TEM images of InP aerogels (Figure 3c and d) show that the material has an interconnected network morphology with an extensive network of pores spanning a range of sizes. Energy-dispersive spectroscopy data for the aerogel suggest a In:P ratio of 1:1.1 and the presence of 4.5% S (Figure S2). The latter is attributed to residual thiolate ligands.

**Surface Area Measurements of InP Nanoparticles and Aerogels.** In order to further probe the porous nature of the network, nitrogen adsorption–desorption isotherms were acquired. Surface areas of InP nanoparticles and aerogels were determined by application of the Brunauer–Emmett–Teller (BET) model, and the pore size distributions were determined using the Barrett–Joyner–Halenda (BJH) model. The adsorption–desorption isotherms of all four samples (3.5 nm NP and AG and 6.0 nm NP and AG) are similar in shape and represent a type IV curve, characteristic of a mesoporous (2–50 nm pore diameter)

material, with a sharp upturn in the high relative pressure region due to liquid condensation in macropores ( $>50$  nm, Figure 4a and b, Figure S3). There was a bimodal distribution of mesopores in both AG samples (insets of Figure 4a and b). These pore size distributions are atypical for aerogels, where a broad range of pores extending from the micro- to the upper macropore region is normally observed and usually what we see for the chalcogenide systems.<sup>5,28</sup> This bimodal distribution, observed consistently from sample to sample, is not evident in TEM micrographs, where the variation in pore size appears continuous.

InP aerogels have comparable surface areas to chalcogenide aerogels of similar mass. The surface areas of the precursor nanoparticles were very low compared to theoretical surface areas; less than 25% of the theoretical surface area was achieved (Table 1). However, by assembling nanoparticles into aerogels we were able to introduce an interconnected pore network, thereby improving the accessible surface area. Thus, more than 60% of the theoretical surface area was achieved for aerogels (Table 1). As expected from our calculations, the 3.5 nm NP and AG samples showed higher surface areas and higher cumulative pore volumes compared to 6.0 nm NP and AG samples (Table 1).

Surprisingly, nanoparticle isotherms also can be modeled by BJH as having a pore size distribution,

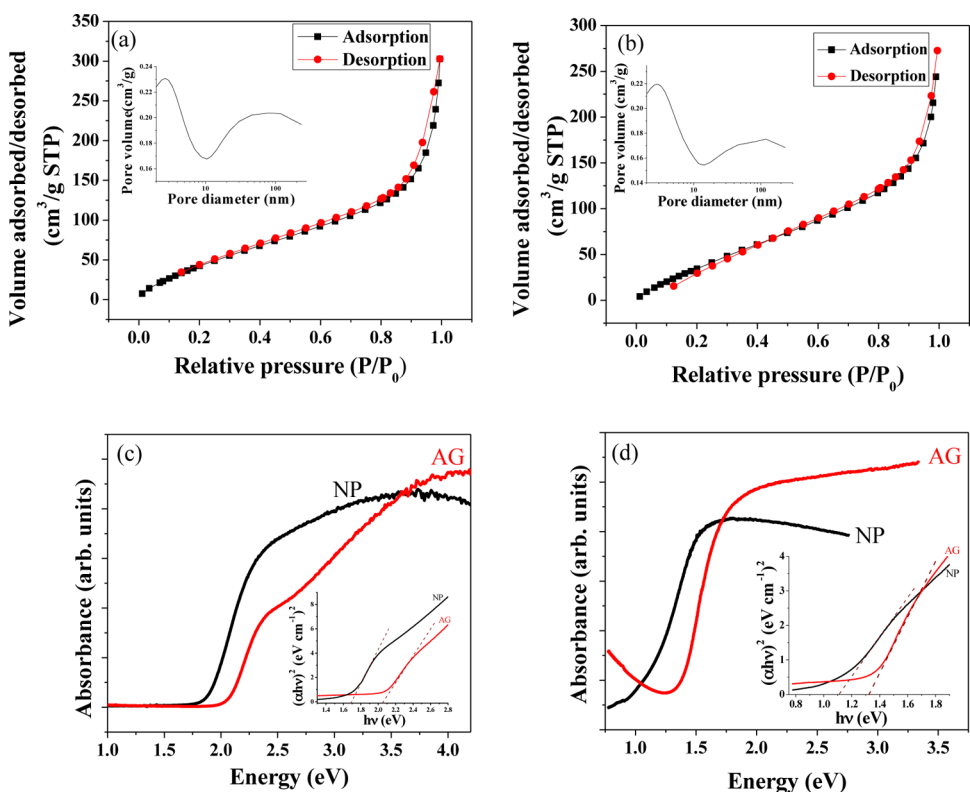


**Figure 4.** Nitrogen adsorption/desorption isotherms for (a) 3.5 nm AG and (b) 6.0 nm AG. The insets of (a) and (b) show the BJH pore size distributions for 3.5 and 6.0 nm AG, respectively. (c, d) Diffuse reflectance UV-visible spectra of 3.5 and 6.0 nm InP NP and AG. The insets of (c) and (d) are the corresponding  $(\alpha h\nu)^2$  vs energy plots ( $\alpha$  = absorbance,  $h$  = Plank's constant, and  $\nu$  = frequency). The x-intercept of the  $(\alpha h\nu)^2$  vs energy plot corresponds to the direct optical band gap of the semiconductor.

**TABLE 1. Theoretical and Experimental Surface Areas; Experimental Pore Sizes and Pore Volumes of NPs and AGs**

sample	theoretical	experimental	average	cumulative
	surface area <sup>a</sup> (m <sup>2</sup> /g)	surface area (m <sup>2</sup> /g)	pore size <sup>b</sup> (nm)	pore volume (cm <sup>3</sup> /g)
3.5 nm NP	356	82	4.8	0.12
3.5 nm AG	356	212	8.7	0.46
6.0 nm NP	208	50	7.0	0.13
6.0 nm AG	208	195	7.7	0.41

<sup>a</sup> Based on the expected surface area of discrete nanoparticles. <sup>b</sup> Average pore size = 4 × total pore volume/total pore area.

but these are largely in the lower mesopore region (<10 nm, Figure S3). This bears some similarity to the first peak in the aerogel pore size distribution plot, but there is no corresponding broader feature at larger pore diameters as observed for aerogels. The appearance of <10 nm pores may be attributable to filling of interstitial spaces or vacant lattice sites within packed nanoparticles.<sup>29</sup> Monodisperse particles, such as those produced here, can adopt close-packed structures, and we do see short-range 2D ordering of InP particles in the TEM (Figure S1). The average pore sizes from surface area analyses are comparable to the average particle size from TEM (~4–8 nm), consistent with the hypothesis that interstitial or vacancy sites are being probed in the former technique.

#### Diffuse Reflectance UV-visible Absorption Measurements of InP Nanoparticles and Aerogels.

In order to discern the effect of assembly on the extent of quantum confinement, diffuse reflectance UV-visible spectroscopy data were acquired on InP nanoparticles and aerogels (Figure 4c and d). We hypothesized that, in keeping with the proposed mechanism of di- or polyphosphide bonding between nanoparticles, we would see a decrease in the band gap upon gel formation due to enhanced delocalization of charge within the network (*i.e.*, the decrease in quantum confinement).

To our surprise, we found that gelation led exclusively to an increase in the band gap. The direct optical band gaps, which were determined from  $(\alpha h\nu)^2$  vs energy plots (insets of Figure 4c and d), for 3.5 nm nanoparticles and the resultant aerogel are 1.7 and 2.1 eV (730 and 590 nm), respectively, and are significantly greater than the band gap of bulk InP (1.35 eV, 919 nm<sup>22</sup>). Similar data are obtained from solution-phase measurements of dispersed InP nanoparticles and InP aerogel aggregates (Figure S4), suggesting the shift in band gap is not due to differences in solid-state packing of the powders for the nanoparticles and aerogels. The blue shift relative to the bulk value of InP suggests that both InP nanoparticles and aerogels are quantum confined. In contrast, the direct band gap values of 6.0 nm nanoparticles and resultant aerogels (~1.1 and 1.35 eV, respectively) are very close to the

bulk band gap (even though this size is far smaller than the reported bulk Bohr exciton diameter of InP, 15 nm<sup>22</sup>). The fact that aerogels demonstrate higher band gap values than their precursor nanoparticles (irrespective of the size) indicates that gelation has resulted in a decrease in the size of the chromophore (*i.e.*, enhanced quantum confinement), despite the fact that they are connected in a 3D linked architecture. Application of the effective mass approximation model to 3.5 nm InP nanoparticles and the resultant aerogels suggests the change in diameter is on the order of 0.5 nm.<sup>30</sup> This is not apparent in crystallite sizes determined from PXRD data because of the lower sensitivity and larger error ( $\pm 0.2$ –0.3 nm) associated with the technique and application of the Scherrer equation. The decrease in chromophore size is in direct contrast to what is observed in metal chalcogenide gels. Brock and co-workers have reported optical band gaps for CdSe nanoparticles, wet gels, aerogels, and xerogels. All of the above-mentioned nanostructures had wider band gaps relative to bulk CdSe. However both aerogels and xerogels of CdSe show a distinct red shift in the band gap relative to the precursor nanoparticles, due to delocalization through the network.<sup>31</sup> This trend has been reported for many other metal chalcogenide systems as well.<sup>10,26</sup> Thus, the blue shift in direct band gap of InP upon gelation suggests a different mechanism is operable in this phosphide system. This has led us to re-evaluate our hypothesis and consider the possibility of surface etching and/or formation of a thick oxidized shell during the process of oxidation with H<sub>2</sub>O<sub>2</sub>.

**Probing the Gelation Mechanism of Metal Phosphides.** Formation of a phosphate/phosphite shell, if it occurred by sacrifice of part of the InP core, would result in an increase in quantum confinement relative to the precursor nanoparticles (Figure 1b). We note that, in contrast to phosphide gels, there is considerable evidence in the literature for phosphate gels. Thus, sol–gel techniques are used to make mesoporous, high surface area amorphous AlPO<sub>4</sub>–SiO<sub>2</sub> and other phosphate gels and glasses.<sup>32,33</sup>

If the hypothesis of oxygenation (Figure 1b) is valid, we expect that use of a non-oxygen-transferring oxidizing agent, such as tetrannitromethane (TNM),<sup>34</sup> would not lead to gelation. Moreover, if phosphates or phosphites are forming, the surface phosphorus will be transformed from a negative to a positive oxidation state, and this change in oxidation state should be evident by X-ray photoelectron spectroscopy (XPS).

Accordingly, we attempted to prepare InP gels using TNM, under air-free conditions, but no gelation was observed. This is in contrast to chalcogenide gelation, which proceeds rapidly with TNM. Surface oxidation of aerogels was confirmed by XPS. Peaks corresponding to In, P, C, and O are all present in both nanoparticle and aerogel samples (Figure S5). High-resolution spectra were also taken for the In 3d and P 2p regions. The In 3d and P

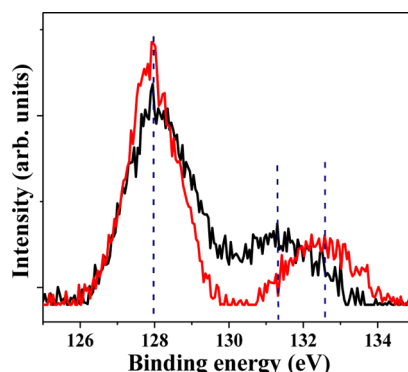


Figure 5. High-resolution XPS spectrum of the P 2p region for TOPO-NP (black) and AG (red).

2p peaks of the aerogel were observed to shift together to a higher binding energy (by 0.87 eV) relative to precursor nanoparticles. This observed shift may be associated with the size reduction of the precursor nanoparticles during gelation (increased quantum confinement effects), or it could be due to the ionization of species prior to the observation of photoemission.<sup>35</sup> Since the In 3d and P 2p peaks characteristic of InP shift together, the shift cannot be due to any change in oxidation state of the observed species. Therefore, we normalized the InP In 3d and P 2p peak positions of aerogels relative to the InP In 3d peak of precursor nanoparticles. These spectra are shown in Figure 5 and Figure S6, respectively, and the original (non-normalized) spectra are shown in Figure S7. In addition to the peak at 127.9 eV corresponding to P from InP, a second peak was observed for TOPO-capped nanoparticles at around 131.2 eV, which we attribute to TOPO on the surface of nanoparticles. This peak is absent in MUA-capped nanoparticles (Figure S8), suggesting TOPO has been displaced during thiolate ligand exchange. In the aerogel, this peak is again absent, and a new peak appears at 132.5 eV, corresponding to an oxidized form of phosphorus that is distinct from, and in higher formal oxidation state than, the phosphorus in TOPO. The oxidized "P" species in the aerogel is attributed to the oxidation of surface phosphorus on InP nanoparticles during gelation, forming phosphorus oxoanions as proposed in Figure 1b. Thus, XPS data are consistent with the formation of phosphate (and/or phosphite) on the surface of nanoparticles during gelation; such species, upon condensation, could lead to formation of P–O–P bonds between particles, resulting in the observed network. There is no evidence for phosphate/phosphite formation in the PXRD of aerogels, suggesting that the oxidized layer formed during gelation is amorphous.

As a final check of our hypothesis, we considered that, if there are P–P bonds between the nanoparticle components of the aerogel, we should be able to disperse InP aerogels using mild reducing agents such as thiolates or phosphines (bond strengths Se–Se < P–P < S–S < P–O), which are successfully used for the

dispersion of metal chalcogenide aerogels. However, metal phosphide gels were not dispersible using MUA or even stronger reducing agents ( $\text{NaBH}_4$ ). Therefore, the oxidation-induced metal phosphide gelation mechanism does not involve P–P bond formation and is not reversible, unlike the case for metal chalcogenide gelation.

## CONCLUSIONS

Sol–gel strategies based on nanoparticle assembly, previously established for metal chalcogenides such as  $\text{CdS}$  and  $\text{CdSe}$ , can be used to interconnect  $\text{InP}$  nanoparticles, leading to a network in which the extent of quantum confinement is increased relative to precursor nanoparticles. The interconnected 3D architectures of

nanoparticles have both meso- and macropores, with accessible surface areas of  $\sim 200 \text{ m}^2/\text{g}$ . XPS studies of nanoparticles and aerogels suggest the formation of a surface phosphate/phosphite, indicating a gelation mechanism based on phosphorus oxoanion condensation, in contrast to related chalcogenide materials, where there is no oxygen incorporation. The high surface area and interconnected pore structure suggest these materials may be useful in applications such as photocatalysis and hybrid photovoltaics. Studies probing the generality of this approach, as well as postmodification strategies to remove oxygen from the interfaces without compromising the network, are under way en route to demonstrating applications of this new class of materials.

## METHODS

**Reagents.** All preparation procedures were carried out under inert atmosphere conditions using an argon-filled glovebox or a Schlenk line, the exception being the thiolate capping and gelation processes, which were carried out in the lab ambient. Indium(III) chloride ( $\text{InCl}_3$ , 99%, Alfa-Aesar), tris(trimethylsilyl)-phosphine ( $\text{P}[\text{Si}(\text{CH}_3)_3]_3$ , 98%, Strem), tris(dimethylamino)-phosphine ( $\text{P}[(\text{CH}_3)_2\text{N}]_3$ , 98%, Strem), pyridine (py, Fisher, 99.9%), chloroform (Fisher, 99.9%), 11-mercaptopoundecanoic acid (MUA, Aldrich 95%), tetramethylammonium hydroxide pentahydrate (Acros, 99%), hydrogen peroxide ( $\text{H}_2\text{O}_2$ , 3%), absolute ethanol (AAPEL Alcohols and Chemicals), and ethyl acetate (Fisher, 99.9%) were used as received. Trioctylphosphine oxide (TOPO, Aldrich, 90%) was distilled prior to use.

**Synthesis of  $\text{InP}$  Nanoparticles.** A method employed by Heath and co-workers was applied, with slight modifications. A rapid injection of a phosphorus precursor (a phosphine) into a hot coordinating solvent (TOPO), in which the indium precursor ( $\text{InCl}_3$ ) is dissolved, causes a rapid nucleation of  $\text{InP}$  nanoparticles, as observed by a reaction color change from colorless to reddish-brown (*ca.* 3–5 min). Although the relatively inexpensive  $\text{P}[(\text{CH}_3)_2\text{N}]_3$  has been reported to yield  $\text{InP}$ , it did not yield any isolable product in our hands, necessitating the use of the more reactive phosphine  $\text{P}[\text{Si}(\text{CH}_3)_3]_3$ .

A solution of tris(trimethylsilyl)phosphine (1.36 mmol) in 1-octadecene (7.0 mL) was injected into a mixture of  $\text{InCl}_3$  (1.36 mmol) and TOPO (5.0 g) preheated at 260 °C for 30–60 min. The nanoparticles were isolated after 24 h of reaction at 260 °C by reducing the reaction temperature to 60 °C followed by dispersion in  $\text{CHCl}_3$  and precipitation with absolute ethanol. The nanoparticles were collected by centrifugation. (Note: the reaction can be carried out at 200 °C, instead of heating at 260 °C, with the same results.)

The synthesis of 6.0 nm  $\text{InP}$  nanoparticles was carried out using a continuous injection method. Briefly, the  $\text{InCl}_3$  (1.36 mmol) was completely dissolved in 7 mL of TOP by slight heating. The phosphorus source, tris(trimethylsilyl)phosphine (1.36 mmol), was mixed with this solution after cooling to room temperature. The mixture, in a syringe attached with a long needle, was injected into hot TOPO (260 °C) at a varying rate profile using a syringe pump. First, 2 mL of solution was injected at a rate of 2 mL/min and the reaction allowed to proceed for 1.5 h; then a 1 mL aliquot was injected at a rate of 1 mL/min. Thereafter, 0.5 mL was injected every 30 min at a rate of 0.5 mL/min. The rest of the reaction procedure is as described for the single injection method.

**Thiolate Exchange of Phosphide Nanoparticles.** The TOPO ligands on the  $\text{InP}$  nanoparticles' surface were subsequently exchanged with 11-mercaptopoundecanoic acid. The amount of MUA used was determined relative to the mole amount of metal precursor used in the nanoparticle synthesis (the targeted metal precursor: MUA ratio was 1:3). The requisite amount of MUA was dissolved in 10–15 mL of absolute ethanol, and the pH was adjusted to

10–11 by the addition of tetramethylammonium hydroxide pentahydrate. Nanoparticles were dispersed in this solution and stirred for 24 h at room temperature under periodic argon flushes. Ethyl acetate was used to wash the MUA-capped nanoparticles and remove excess MUA and TOPO. Thiolate-capped nanoparticles were dispersed in 2–4 mL of absolute ethanol for gelation.

**Wet Gel Formation and Aerogel Preparation.** Wet gel formation was conducted through oxidative sol–gel assembly by using an aqueous solution of 3%  $\text{H}_2\text{O}_2$ . The MUA-capped  $\text{InP}$  nanoparticles were dispersed in absolute ethanol (*ca.* 2–4 mL) in a polyethylene vial under ambient conditions. Dispersion was assisted with sonication (*ca.* 5 min). Then 0.1–0.5 mL of the oxidant, 3%  $\text{H}_2\text{O}_2$ , was mixed with the solution by vigorous shaking, and the solution was allowed to sit until gelation occurred. The gelation starts after *ca.* 30–60 min, and gels were aged for 10–14 days. Prior to the liquid  $\text{CO}_2$  exchange and supercritical drying, the gel solvent was thoroughly exchanged with 3–5 mL aliquots of acetone without disturbing the gel network. This was done three times over at least 3–4 days. In each exchange cycle, fresh acetone was used. The wet gel was subsequently transferred to a porous capsule, taking care not to disturb the gel structure. Sample capsules were loaded in the drying boat and inserted into the critical point dryer (a SPI DRY model) maintained at 19 °C. Solvent exchange was carried out at 19 °C by alternatively filling the sample chamber with liquid  $\text{CO}_2$  and draining the  $\text{CO}_2$ , in one-hour intervals, over a time period of 4 h. For the supercritical drying step, the chamber was filled halfway with liquid  $\text{CO}_2$  followed by a temperature increase to 39 °C. With the increase of the temperature, the pressure inside the chamber increased (1300–1500 psi). The gel was kept at that temperature and pressure for 1 h, and then the pressure was released to dry the gel.

**Characterization.** *Powder X-ray Diffraction.* A Rigaku RU 200B X-ray diffractometer with a  $\text{Cu K}\alpha$  rotating anode source was employed to study the phase and crystallinity of the nanoparticles and aerogels. The vacuum-dried samples were deposited on a low-background quartz (0001) holder coated with a thin layer of grease. X-ray diffraction patterns were identified by comparison to phases in the International Centre for Diffraction Data (ICDD) powder diffraction file (PDF) database (release 2000).

**Transmission Electron Microscopy.** A JEOL 2010 HR TEM electron microscope operating at an accelerating voltage of 200 kV and a current of 106–108  $\mu\text{A}$  with a coupled EDS detector (EDAX Inc.) was employed to study the morphology and composition of nanoparticles and aerogels. Nanoparticle samples were prepared by placing a drop of a dilute chloroform dispersion of nanoparticles on a carbon-coated copper grid and evaporating the solvent. Aerogel samples were made by grinding the aerogel to a fine powder and pressing the carbon-coated grid onto the powder.

**Surface Area Analysis and Porosimetry.** A Micromeritics TriStar II 3020 surface area analyzer was used for surface area and pore size analysis. The surface areas of nanoparticles (vacuum-dried) and aerogels were obtained by applying the Brunauer–Emmett–Teller model to nitrogen adsorption–desorption isotherms acquired at 77 K. Samples were degassed at 150 °C for 24 h prior to the analysis. The Barrett–Joyner–Halenda model was employed to analyze the pore size distribution of aerogels.

**Optical Absorption Measurements.** A Jasco V-570 UV/vis/NIR spectrometer equipped with an integrating sphere was employed to measure the optical diffuse reflectance of the nanoparticles and aerogels. The powder samples were evenly spread on a sample holder with a reflectance standard ( $\text{BaSO}_4$ ) and measured from 200 to 1000 nm (1.24–6.20 eV). The baseline was corrected by a reflectance standard ( $\text{BaSO}_4$ ). The Kubelka–Munk equation was used to convert the reflectance data to absorbance. The absorbance spectra for InP nanoparticles and aerogels were replotted according to  $\alpha = C(h\nu - E_g^{\text{bulk}})^{1/2}/h\nu$  (where  $\alpha$  is the absorption coefficient,  $C$  is a constant,  $h\nu$  is photon energy, and  $E_g^{\text{bulk}}$  is bulk band gap), and the direct optical band gap of the semiconductor was obtained from the  $x$ -intercept of the  $(\alpha h\nu)^2$  vs energy plot.

**X-ray Photoelectron Spectroscopy.** A PerkinElmer PHI 5500 with a monochromatic  $\text{Al K}\alpha$  X-ray radiation source (1486.6 eV) and an Auger-Scan system control (RBD Enterprises, Bend, OR, USA) was employed. The samples were prepared by pressing powder samples onto a piece of indium foil. Survey scans were collected to 1200 eV, with a 1 eV/step resolution. High-resolution scans were collected over a range of 125–137 eV (for P 2p) and 440–448 eV (for In 3d). To prevent any possibility of adventitious oxidation of nanoparticles and aerogels, the samples were handled under air-free conditions except for the rapid transfer to the XPS chamber.

**Conflict of Interest:** The authors declare no competing financial interest.

**Acknowledgment.** This work has been supported by funds from the National Science Foundation (DMR-0094213 (CAREER), DMR-0701161, and DMR-1064159). We thank C. M. Thrush for help with the XPS studies.

**Supporting Information Available:** TEM, EDS, nitrogen adsorption–desorption isotherms, and BJH pore size distributions of InP nanoparticles, EDS spectra of aerogels, UV–vis absorbance and XPS survey spectra of TOPO-capped nanoparticles and corresponding aerogels, and high-resolution XPS spectra for TOPO- and MUA-capped nanoparticles and corresponding aerogels. This material is available free of charge via the Internet at <http://pubs.acs.org>.

## REFERENCES AND NOTES

- Hüsing, N.; Schuber, U. Aerogels-Airy Materials: Chemistry, Structure and Properties. *Angew. Chem., Int. Ed.* **1998**, *37*, 22–45.
- Pekala, R. W. Organic Aerogels from the Polycondensation of Resorcinol with Formaldehyde. *J. Mater. Sci.* **1989**, *24*, 3221–3227.
- Rolison, D. R.; Long, J. W.; Lytle, J. C.; Fischer, A. E.; Rhodes, C. P.; McEvoy, T. M.; Bourga, M. E.; Lubersa, A. M. Multi-functional 3D Nanoarchitectures for Energy Storage and Conversion. *Chem. Soc. Rev.* **2009**, *38*, 226–252.
- King, J. S.; Wittstock, A.; Biener, J.; Kucheyev, S. O.; Wang, Y. M.; Baumann, T. F.; Giri, S. K.; Hamza, A. V.; Baeumer, M.; Bent, S. F. Ultralow Loading Pt Nanocatalysts Prepared by Atomic Layer Deposition on Carbon Aerogels. *Nano Lett.* **2008**, *8*, 2405–2409.
- Worsley, M. A.; Pauzauskie, P. J.; Olson, T. Y.; Biener, J.; Satcher, J. H.; Baumann, T. F. Synthesis of Graphene Aerogel with High Electrical Conductivity. *J. Am. Chem. Soc.* **2010**, *132*, 14067–14069.
- Mulik, S.; Sotiriou-Leventis, C.; Leventis, N. Time-Efficient Acid-Catalyzed Synthesis of Resorcinol–Formaldehyde Aerogels. *Chem. Mater.* **2007**, *19*, 6138–6144.
- Mohanan, J. L.; Brock, S. L. A New Addition to the Aerogel Community. *J. Non-Cryst. Solids* **2004**, *350*, 1–8.
- Mohanan, J. L.; Arachchige, I. U.; Brock, S. L. Porous Semiconductor Chalcogenide Aerogels. *Science* **2005**, *307*, 397–400.
- Yao, Q.; Brock, S. L. Porous CdTe Nanocrystal Assemblies: Ligation Effects on the Gelation Process and the Properties of Resultant Aerogels. *Inorg. Chem.* **2011**, *50*, 9985–9992.
- Arachchige, I. U.; Brock, S. L. Sol-Gel Methods for the Assembly of Quantum-Dot Monoliths. *Acc. Chem. Res.* **2007**, *40*, 801–809.
- Kalebaila, K. G.; Brock, S. L. Synthesis and Characterization of Germanium Sulfide Aerogels. *J. Non-Cryst. Solids* **2006**, *352*, 232–240.
- Bag, S.; Kanatzidis, M. G. Chalcogels: Porous Metal–Chalcogenide Networks from Main-Group Metal Ions. Effect of Surface Polarizability on Selectivity in Gas Separation. *J. Am. Chem. Soc.* **2010**, *132*, 14951–14959.
- Oh, Y.; Morris, C. D.; Kanatzidis, M. G. Polysulfide Chalcogels with Ion-Exchange Properties and Highly Efficient Mercury Vapor Sorption. *J. Am. Chem. Soc.* **2012**, *134*, 14604–14608.
- Polychronopoulou, K.; Malliakas, C. D.; He, J.; Kanatzidis, M. G. Selective Surfaces: Quaternary Co(Ni)MoS-Based Chalcogels with Divalent ( $\text{Pb}^{2+}$ ,  $\text{Cd}^{2+}$ ,  $\text{Pd}^{2+}$ ) and Trivalent ( $\text{Cr}^{3+}$ ,  $\text{Bi}^{3+}$ ) Metals for Gas Separation. *Chem. Mater.* **2012**, *24*, 3380–3392.
- Gill, S. K.; Hope-Weeks, L. J. Monolithic Aerogels of Silver Modified Cadmium Sulfide Colloids. *Chem. Commun.* **2009**, *29*, 4384–4386.
- Gaponik, N.; Wolf, A.; Marx, R.; Lesnyak, V.; Schilling, K.; Eychmüller, A. Three-Dimensional Self-Assembly of Thiol-Capped CdTe Nanocrystals: Gels and Aerogels as Building Blocks for Nanotechnology. *Adv. Mater.* **2008**, *20*, 4257–4262.
- Lesnyak, V.; Voitekhovich, S. V.; Gaponik, P. N.; Gaponik, N.; Eychmüller, A. CdTe Nanocrystals Capped with a Tetrazolyl Analogue of Thioglycolic Acid: Aqueous Synthesis, Characterization, and Metal-Assisted Assembly. *ACS Nano* **2010**, *4*, 4090–4096.
- Bag, S.; Gaudette, A. F.; Bussell, M. E.; Kanatzidis, M. G. Spongy Chalcogels of Non-Platinum Metals Act as Effective Hydrodesulfurization Catalysts. *Nat. Chem.* **2009**, *1*, 217–224.
- Bag, S.; Arachchige, I. U.; Kanatzidis, M. G. Aerogels from Metal Chalcogenides and Their Emerging Unique Properties. *J. Mater. Chem.* **2008**, *18*, 3628–3632.
- Lange, S.; Bawohl, M.; Weihrich, R.; Nilges, T. Mineralization Routes to Polyphosphides:  $\text{Cu}_2\text{P}_{20}$  and  $\text{Cu}_5\text{InP}_{16}$ . *Angew. Chem., Int. Ed.* **2008**, *47*, 5654–5657.
- Kraus, F.; Korber, N. The Chemical Bond in Polyphosphides: Crystal Structures, the Electron Localization Function, and a New View of Aromaticity in  $\text{P}_4^{2-}$  and  $\text{P}^{5-}$ . *Chem.—Eur. J.* **2005**, *11*, 5945–5959.
- Guzelian, A. A.; Katari, J. E. B.; Kadavanich, A. V.; Banin, U.; Hamad, K.; Juban, E.; Alivisatos, A. P.; Wolters, R. H.; Arnold, C. C.; Heath, J. R. Synthesis of Size-Selected, Surface-Passivated InP Nanocrystals. *J. Phys. Chem.* **1996**, *100*, 7212–7219.
- Duan, X.; Huang, Y.; Cui, Y.; Wang, J.; Lieber, C. M. Indium Phosphide Nanowires as Building Blocks for Nanoscale Electronic and Optoelectronic Devices. *Nature* **2001**, *409*, 66–69.
- Wang, J.; Gudiksen, M. S.; Duan, X.; Cui, Y.; Lieber, C. M. Highly Polarized Photoluminescence and Photodetection from Single Indium Phosphide Nanowires. *Science* **2001**, *293*, 1455–1457.
- Minot, E. D.; Kelkensberg, F.; van Kouwen, M.; van Dam, J. A.; Kouwenhoven, L. P.; Zwoller, V.; Borgstrom, M. T.; Wunnicke, O.; Verheijen, M. A.; Bakkers, E. P. Single Quantum Dot Nanowire LEDs. *Nano Lett.* **2007**, *7*, 367–371.
- Pala, I. R.; Arachchige, I. U.; Georgiev, D. G.; Brock, S. L. Reversible Gelation of II–VI Nanocrystals: The Nature of Interparticle Bonding and the Origin of Nanocrystal Photochemical Instability. *Angew. Chem., Int. Ed.* **2010**, *49*, 3661–3665.
- Hoffmann, R.; Zheng, C. Making and Breaking Bonds in the Solid State: The  $\text{ThCr}_2\text{Si}_2$  Structure. *J. Phys. Chem.* **1985**, *89*, 4175–4181.

28. Arachchige, I. U.; Brock, S. L. Sol-Gel Assembly of CdSe Nanoparticles to form Porous Aerogel Networks. *J. Am. Chem. Soc.* **2006**, *128*, 7964–7971.
29. Muthuswamy, E.; Brock, S. L. Solid-State Phase Transformations in Solution: Templated Conversion of Nanoscale Nickel Phosphides. *Chem. Commun.* **2011**, *47*, 12334–12336.
30. Pesika, N. S.; Stebe, K. J.; Searson, P. C. Determination of the Particle Size Distributions of Quantum Nanocrystals from Absorbance Spectra. *Adv. Mater.* **2003**, *15*, 1289–1291.
31. Yu, H.; Liu, Y.; Brock, S. L. Tuning the Optical Band Gap of Quantum Dot Assemblies by Varying Network Density. *ACS Nano* **2009**, *3*, 2000–2006.
32. Araujo, C.; Zhang, L.; Eckert, H. Sol-Gel of AlPO<sub>4</sub>-SiO<sub>2</sub> Glasses with Higher Surface Area Mesopore Structure. *J. Mater. Chem.* **2006**, *16*, 1323–1331.
33. Zhang, L.; Eckert, H. Sol-Gel Synthesis of Al<sub>2</sub>O<sub>3</sub>-P<sub>2</sub>O<sub>5</sub> Glasses: Mechanistic Studies by Solution and Solid State NMR. *J. Mater. Chem.* **2004**, *14*, 1605–1615.
34. Evans, B. H.; Doi, J. T.; Musker, W. K. Fluorine-19 NMR Study of the Reaction of *p*-Fluorobenzenethiol and Disulfide with Periodate and other Selected Oxidizing Agents. *J. Org. Chem.* **1990**, *55*, 2337–2344.
35. Katari, J. E. B.; Colvin, V. L.; Alivisatos, A. P. X-ray Photoelectron Spectroscopy of CdSe Nanocrystals with Applications to Studies of the Nanocrystal Surface. *J. Phys. Chem.* **1994**, *98*, 4109–4117.